Synchronous Diagnosis of Respiratory Viruses Variants via Receptonics Based on Modeling Receptor–Ligand Dynamics

Sung Eun Seo, Kyung Ho Kim, Siyoung Ha, Hanseul Oh, Jinyeong Kim, Soomin Kim, Lina Kim, Minah Seo, Jai Eun An, Yoo Min Park, Kyoung G. Lee, Yu Kyung Kim, Woo-Keun Kim, Jung Joo Hong,* Hyun Seok Song,* and Oh Seok Kwon*

The transmission and pathogenesis of highly contagious fatal respiratory viruses are increasing, and the need for an on-site diagnostic platform has arisen as an issue worldwide. Furthermore, as the spread of respiratory viruses continues, different variants have become the dominant circulating strains. To prevent virus transmission, the development of highly sensitive and accurate on-site diagnostic assays is urgently needed. Herein, a facile diagnostic device is presented for multi-detection based on the results of detailed receptor–ligand dynamics simulations for the screening of various viral strains. The novel bioreceptor-treated electronics (receptonics) device consists of a multichannel graphene transistor and cell-entry receptors conjugated to N-heterocyclic carbene (NHC). An ultrasensitive multi-detection performance is achieved without the need for sample pretreatment, which will enable rapid diagnosis and prevent the spread of pathogens. This platform can be applied for the diagnosis of variants of concern in clinical respiratory virus samples and primate models. This multi-screening platform can be used to enhance surveillance and discriminate emerging virus variants before they become a severe threat to public health.

1. Introduction

Since the 2019 outbreak of the novel coronavirus SARS-CoV-2, which causes COVID-19, the virus has spread from its origin in China to at least 215 countries, generating various mutant strains that have been monitored as variants of concern (VOC).[1] The WHO has outlined key criteria to designate VOCs: transmissibility, disease severity, risk of reinfection, and impacts on diagnostics and vaccine performance. Depending on those criteria, circulating variants may be reclassified.[2] The surveillance of SARS-CoV-2 strains is highly important for building a collection of SARS-CoV-2 specimens and maintaining public health.[3] Various SARS-CoV-2 lineages have been categorized by the World Health Organization (WHO) as VOCs, including B.1.1.7 (Alpha), B.1.351 (Beta), P.1 (Gamma), and B.1.617.2 (Delta).[4] Each class possesses

S. E. Seo, K. H. Kim, S. Ha, J. Kim, S. Kim, L. Kim, J. E. An
Infectious Disease Research Center
Korea Research Institute of Bioscience and Biotechnology (KRIBB)
125 Gwahak-ro, Yuseong-gu, Daejeon 34141, Republic of Korea
S. E. Seo, S. Kim
Department of Civil and Environmental Engineering
Yonsei University
Seoul 03722, Republic of Korea
K. H. Kim
Immunotherapy Research Center
Korea Research Institute of Bioscience and Biotechnology (KRIBB)
Daejeon 34141, Republic of Korea
S. Ha
School of Pharmacy
University of Maryland Eastern Shore
Princess Anne, MD 21853, USA
H. Oh
College of Veterinary Medicine
Chungbuk National University
Cheongju 28644, Republic of Korea

M. Seo, H. S. Song
Sensor System Research Center
Korea Institute of Science and Technology
Seoul 02792, Republic of Korea
E-mail: hssong@kist.re.kr
M. Seo
KU-KIST Graduate School of Converging Science and Technology
Korea University
Seoul 02841, Republic of Korea
Y. M. Park, K. G. Lee
Center for NanoBio Development
National NanoFab Center
291 Daehak-ro, Yuseong-gu, Daejeon 34141, Republic of Korea
Y. K. Kim
Department of Clinical Pathology
School of Medicine
Kyungpook National University
Daegu 41944, Republic of Korea
W.-K. Kim
Department of Predictive Toxicology
Korea Institute of Toxicology
141 Gajeong-ro, Yuseong-gu, Daejeon 34114, Republic of Korea

**ADVANCED
SCIENCE NEWS**

www.advancedsciencenews.com

**ADVANCED
MATERIALS**

www.advmat.de

mutations in the S protein. Among various lineages, the first VOC, Alpha (B.1.1.7), initially appeared in England in September 2020. The B.1.1.7 lineage was 30 to 50% more contagious than the original SARS-CoV-2 strain.[5] In October 2020, another variant, the B.1.617 lineage (Delta), was reported, overtaking the Alpha lineage.[6] As new variants increase in prevalence and become the predominant lineage due to their increased transmissibility compared to the previous dominant variant, new waves of infection occur globally.[6] The mutant strains showed greater replication ability and more efficient spread (transmissibility), as well as enhanced vaccine- resistance compared with the original strain of the virus.[7,8] The currently circulating VOC is Omicron (B.1.1.529), which was designated the fifth VOC in November 2021.[9]

Several methodologies have been developed for the diagnosis of respiratory viruses and the identification of its variants. Nevertheless, these conventional immunoassays and molecular diagnostics have several limitations; for example, they must be performed by trained professionals, they require large volumes of samples, and their operation times are long.[10] Those disadvantages were considered as hurdles to the prevention of the rapid spread of contagious virus. Herein, we suggest a specific receptor–ligand binding reaction-based receptonics platform to overcome and supplement the limitations of existing methodologies. Since person-to-person transmission of respiratory virus occurs through the interaction of the receptor binding domain (RBD) of the virus with a human receptor,[11,12] we focused on the electrical signal amplification by the immobilized receptors onto the graphene transistor. It is noted that three different types of respiratory infectious viruses including influenza virus, rhinovirus, and coronavirus were clearly discriminated by assistance of three receptors (ACE2, neuropilin-1, and DPP4). Among numerous strains of coronavirus, different species are distinguished depending on the signal from different receptor-immobilized transistors. MERS-CoV (DPP4) and SARS-CoV (ACE2) react to specific receptors.[13,14] Moreover, SARS-CoV-2 reacts with ACE2 and neuropilin-1 with different binding affinities.[15,16,17] Variants of SARS-CoV-2 show differences in infection rates compared to wildtype viruses.[18,19,20] Mutations in the spike protein RBD substantially increase the binding affinity of the RBD-hACE2 complex, and this increase is related to the rapid spread of the virus.[21] Herein, we exploited the various binding affinities of variants of the virus to discriminate the species. The electrical signal generated by the receptonics device upon virus detection can be compared to the molecular interactions modelled in previous research with reasonable correlations.

We first developed a portable electrochemical biosensor based on a ligand–receptor binding reaction. This diagnostic device has various advantages compared to conventional diagnostics, such as the ability to recognize multiple viruses, applicability to nasal samples without requiring pretreatment, superior detection performance, ability to compare various receptors, and detection of clinical samples using a stable chemical linker (N-heterocyclic carbene) conjugated to the receptor. The screening platform for the simultaneous diagnosis of various species of virus (influenza virus or coronavirus) was realized based on the fabrication of a multichannel transistor micropatterned on a miniaturized electrode. In addition, a comparison of the binding affinities of various receptors to SARS-CoV-2 was conducted with simulation data. Based on the results, it was possible to discriminate among variants and compare the infection rates of different mutant strains. In addition, the newly developed interface chemistry was applied to COVID-19-infected clinical samples and samples from a primate model. The surface protection effect of N-heterocyclic carbene effectively lowers the interference effect. Thus, false-positive signals caused by biomaterials contained in the nasal swabs were minimized, in contrast to the case treated with conventional diagnosis methodologies. The cohort study was performed among individuals with laboratory-confirmed COVID-19 in South Korea. Also, potential cases of reinfection were included to confirm the effect of the lineage on the binding affinity. Simulation was used to estimate the ligand–receptor binding affinities for the wild-type variant compared with the Alpha and Delta variants. The advantages of the screening platform, such as its long-term stability, portability, and multiplexing capability for the measurement, diagnosis, and screening of respiratory viruses and their variants, indicate its potential as an on-site screening platform for fatal diseases without the need for complex additional equipment (**Scheme 1**).

J. J. Hong
National Primate Research Center
Korea Research Institute of Bioscience and Biotechnology
Cheongju 28116, Republic of Korea
E-mail: hong75@kribb.re.kr

J. J. Hong
KRIBB School of Bioscience
Korea University of Science & Technology (UST)
Daejeon 34141, Republic of Korea

O. S. Kwon
SKKU Advanced Institute of Nanotechnology (SAINT)
Department of Nano Engineering
Sungkyunkwan University
Suwon 16419, Republic of Korea
E-mail: oskwon79@skku.edu

O. S. Kwon
Department of Nano Science and Technology
Sungkyunkwan University
Suwon 16419, Republic of Korea

2. Results and Discussion

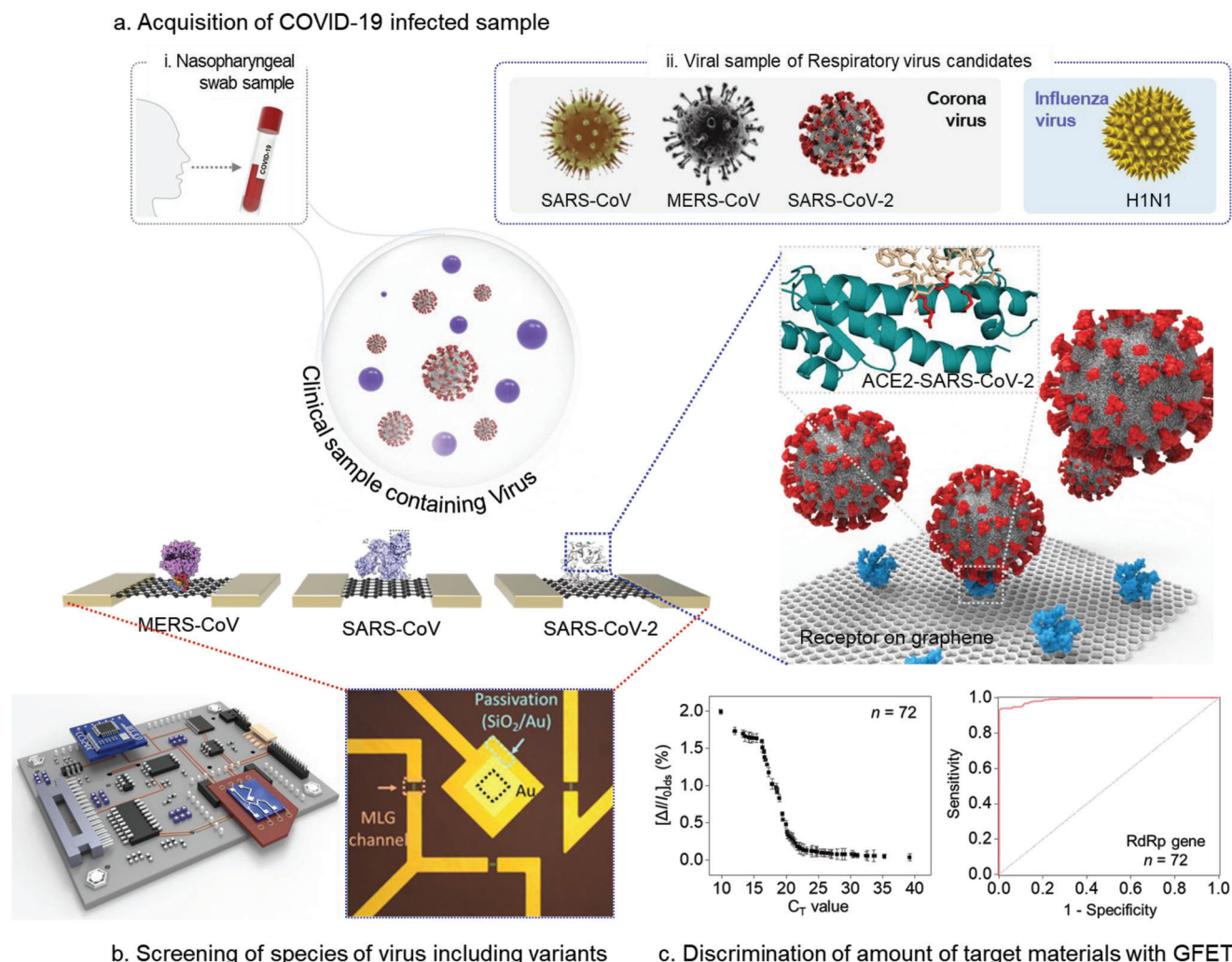### 2.1. Characterization of NHC Introduction onto MLG

To investigate the theoretical confirmation of the covalent bonding energy between N-heterocyclic carbene (NHC) and the graphene micropattern (GM), density functional theory (DFT) was applied to obtain the 3D structures of the electron density difference map (EDDM), the highest occupied molecular orbital (HOMO), and the lowest unoccupied molecular orbital (LUMO) (**Figure 1**a). EDDM showed electron transfer from the NHC to the GM, which indicates the doping effect of the covalent bonding between the NHC and GM. The interaction energy was calculated with the following equation:[22,23]

$$\Delta E_{int} = E_b - \left[E_{GM} + E_{NHC} \right] \tag{1}$$

Scheme 1. Schematic illustration of the overall process of synchronous diagnosis with a cell-entry receptor-immobilized multiple graphene channel-based receptonics device.

In Equation (1), E_b is the energy of the interacting state and E_{GM} and E_{NHC} are the absolute energy of each material (graphene and NHC, respectively). Based on these results, the interaction energy was confirmed to be $-29\,162.1$ eV, which is characterized as high energy. The orbital energy gap (OEG) was obtained from the calculated HOMO (-3.687 eV) and LUMO (-2.194 eV) energies. Thus, the opened bandgap formed by covalent bonding between the unshared electron pairs in NHC and graphene was calculated as -1.493 eV.[24] In addition, electron transfer between the NHC and the GM was confirmed through EDDM, which means the possibility of electron transfer from NHC to GM (Figure S1, Supporting Information).

Cs-corrected high-resolution scanning transmission electron microscopy (Cs-STEM) analysis was performed to investigate the surface variance before and after NHC introduction onto monolayer graphene (MLG). The surface image showed the honeycomb shape (yellow dot) of MLG, and the selected-area electron diffraction (SAED) image was indicative of a typical hexagonal pattern and (111) plane (Figure 1b; Figure S2a, Supporting Information).[23,25] MLG was prepared for the formation of cova-

lent bonds with NHC to confirm the (111) plane in MLG.[26,27,28] After NHC introduction on MLG, the lattice pattern was changed from hexagonal to trapezoid (blue dot) shape by the covalent bonding (Figure 1c). The diffraction pattern showed an additional pattern next to the (111) plane of MLG (Figure S2b, Supporting Information). The conjugation of NHC was proven by the increased thickness after NHC conjugation of 40 Å (blue line in Figure 1c) compared with pristine MLG (9 Å, yellow line in Figure 1b) by profiling of Cs-STEM images (Figure S3, Supporting Information).

Moreover, Raman spectroscopy analysis was performed to confirm the variance of the molecular interaction and crystallinity depending on the covalent bond formed by the introduction of NHC onto MLG. The distinct 2D (2639 cm^{-1}) and G (1588 cm^{-1}) peaks due to the high frequency of the E_{2g} phonon were indicated by the close ideal monolayer (black line) as ca. double ($I_{2D}/I_G \approx 1.99$) that in the spectrum of pristine MLG (Figure 1d).[29,30,31] In addition, a weak D + D** band (2480 cm^{-1}) was observed upon defect activation by visible light.[32] After the introduction of NHC (red line), a broad D peak was generated between 1280–1360 cm^{-1}

**ADVANCED
SCIENCE NEWS**

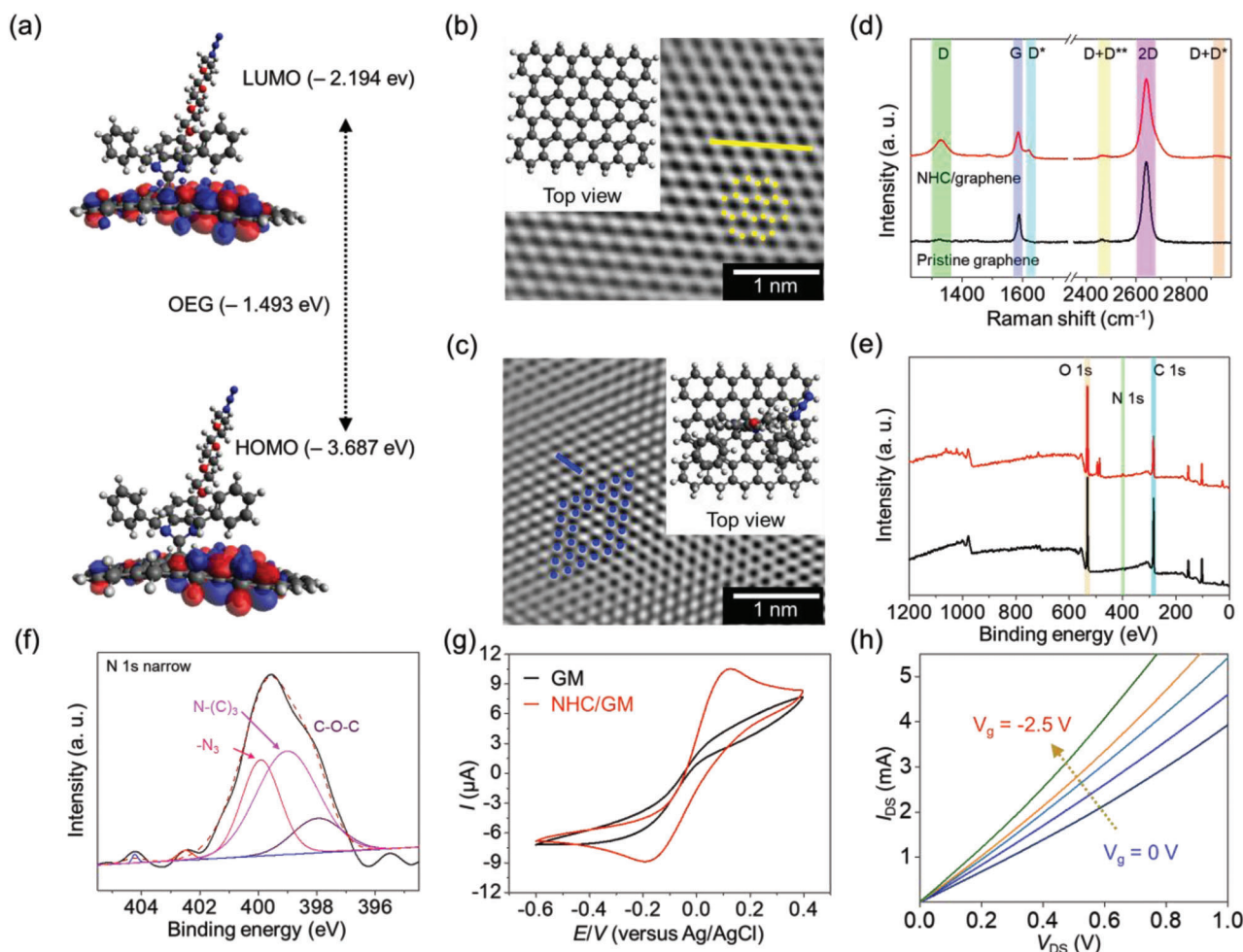www.advancedsciencenews.com

**ADVANCED
MATERIALS**

www.advmat.de

Figure 1. Surface modification with N-heterocyclic carbenes. a) 3D structures of the HOMO and LUMO states of NHC/GM. b,c) Cs-STEM images before (b) and after (c) NHC introduction on GM. d) Raman spectra and e) XPS spectra depending on NHC introduction; f) fitted N 1s narrow spectrum. g) CV curves toward the reduction/oxidation of Fc-conjugated NHC/GM in NaClO₄ solution. h) Output curves of NHC/GM to confirm the gating effect.

due to the defect activation of the hexagonal atom rings.[33] The D* peak (1620 cm⁻¹) was observed beside the G peak owing to defect generation by NHC bonding.[34] A broad band at 2940 cm⁻¹ representing the D + D* peak appeared due to the defect from the emitted intervalley phonon.[35]

To investigate the covalent bond between NHC and graphene, binding energy analysis between atoms was performed using X-ray photoelectron spectroscopy (XPS) (Figure 1e). Survey scan spectra exhibited before and after NHC introduction on graphene, and there were no observations of impurities.[23] Two peaks, C 1s and O 1s indicated pristine graphene, and were increased in the NHC/Gr graph owing to the heterocycle ring, aromatic ring, and poly(ethylene glycol) group (PEG) of the NHC terminus. In addition, the N 1s core level was obviously present at 402 to 396.5 eV due to the azide group (400.1 eV) of the functional group and N—(C)₃ (398.8 eV) in the heterocyclic ring after NHC introduction, demonstrating the surface functionalization of the graphene (Figure 1f).[36,37]

Electrochemical analysis (cyclic voltammetry: CV) was carried out to determine the amount of covalently bonded NHC. The oxidation and reduction peaks were confirmed at 0.31 V and −0.42 V,

respectively (Figure 1g). The amount of NHC-based covalent bonds from the CV results was measured as 2.9336 mol nm⁻² through the area integral and was calculated based on Faraday's law (Figure S4, Supporting Information). In addition, the opened-bandgap-based NHC/GM was fabricated as electrodes to embody the field-effect transistor (FET) system (Figure 1h). The output curve (I_{DS}–V_{DS}) was measured to confirm the gating effect in the gate voltage range of 0 to −2.5 V (sweep: −0.1 V) in dielectric materials (pH 7.0 PBS). The electrical property showed a gating effect and p-type characterization, with the increasing negativity of I_{ds} depending on the increased negativity of V_g. The confirmation of p-type operation is a particularly important point for biosensor application owing to the effect of the radical formed from the channel surface of n-type materials on biomolecules.

2.2. Receptonics Performance Evaluation

A photograph in **Figure 2**a shows the multichannel receptonics device, which is composed of source, 3-drain, and coplanar-gate electrodes. The Au electrode was passivated by the SiO₂ layer to
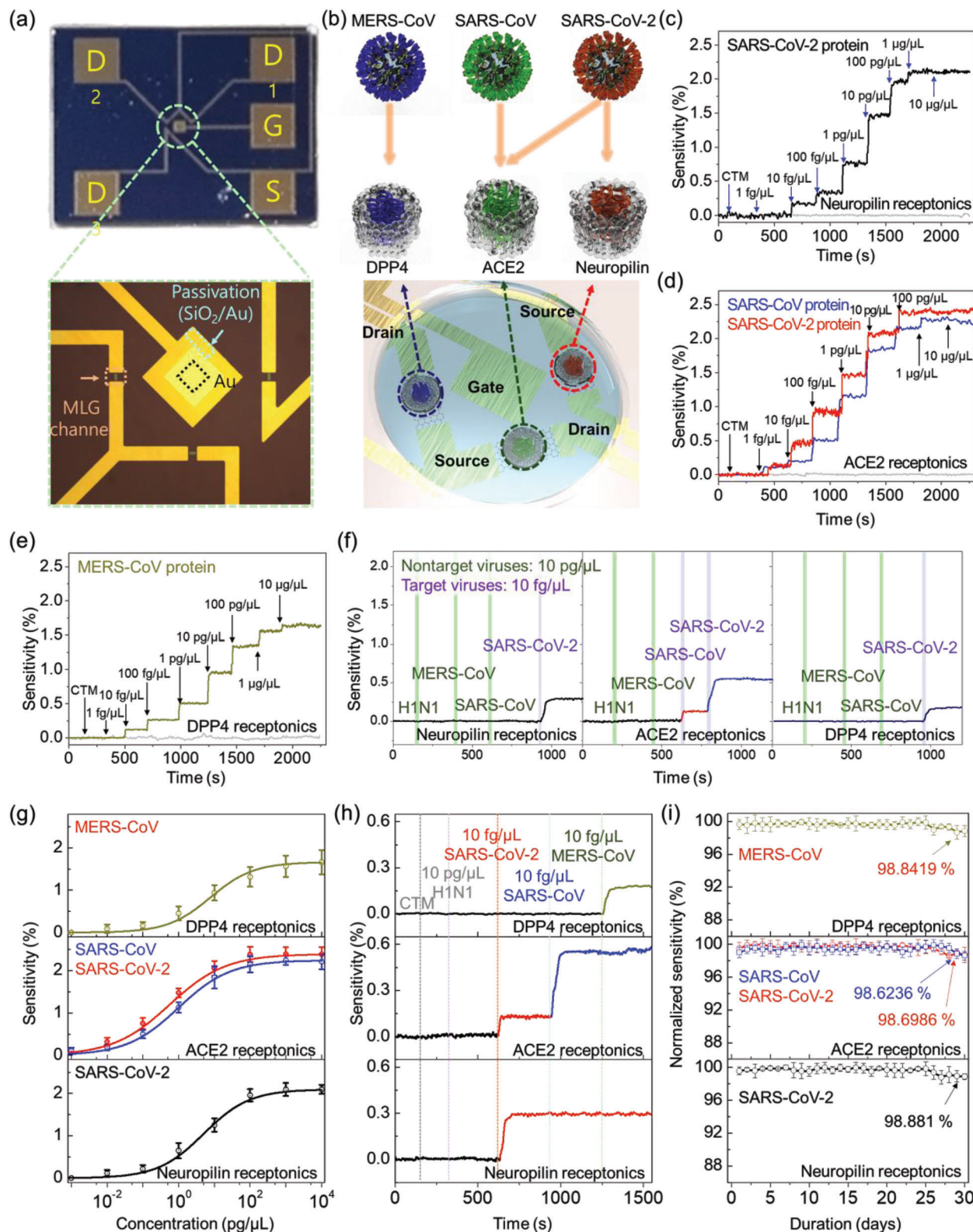
**ADVANCED
SCIENCE NEWS**

www.advancedsciencenews.com

**ADVANCED
MATERIALS**

www.advmat.de

Figure 2. a) Multichannel receptonics consisting of 3 kinds of NDs (neuropilin-1, ACE2, DPP4) and a source, drain, and side-gate for real-time monitoring. b–e) Real-time monitoring of the neuropilin-1 receptor for SARS-CoV-2 (c), the ACE2 receptor for SARS-CoV/SARS-CoV-2 (d), and the DPP4 receptor for MERS-CoV (e). e) Selectivity test of each receptonics using the various respiratory viruses. f) Real-time monitoring of the time-dependent exposures to various respiratory viruses in the multichannel receptonics device. g) Dose–concentration curve for each receptor. h) Selectivity test of each receptonics device. i) Long-term stability of each device for 30 days.

2303079 (5 of 12)

ADVANCED
SCIENCE NEWS

www.advancedsciencenews.com

ADVANCED
MATERIALS

www.advmat.de

prevent noise caused by nonspecific binding, and each channel and the center area of the gate electrode were exposed to bind each nanodisc (ND) supplying gate voltage, as shown in the enlarged image. The illustration in Figure 2b shows the nanodisc-conjugated electrodes and the filling of the chamber with dielectric liquid for field-effect formation by the gate voltage supply. The distances between the source/drain and coplanar-gate electrodes were designed by optimizing for the uniformity of the field effect. The top images show each nanodisc and its specific target viruses. It has been well-established that MERS-CoV binds to the human dipeptidyl peptidase 4 (hDPP4), SARS-CoV binds to the human angiotensin-converting enzyme 2 (hACE2) and SARS-CoV-2 binds to the ACE2 receptor and neuropilin-1.[38,39,40] The SARS-CoV-2 binds more strongly to the ACE2 than SARS-CoV, and ACE2-expressed cells can be infected by SARS-CoV-2 but not those expressing DPP4 (Table S1, Supporting Information). Furthermore, neuropilin-1 (NRP1), known to bind to furin cleavage substrates was abundantly expressed in almost all pulmonary and olfactory cells, significantly potentiates SARS-CoV-2 infectivity and the COVID-19-infected olfactory epithelial cells has high expression of NRP1.[17,41] Therefore, for the high selectivity of the sensing platform, we used three type of the nanodisc (DPP4, ACE2, and NRP1) as human target receptor. In this study, ACE2, DPP4, and NRP1 were produced using an *Escherichia coli* cell system and incorporated in nanodisc structures by the experimental procedure described in our previous works.[23,42,43]

Figure 2c,e show the real-time responses of the detection to different concentrations of each virus spike protein. Before signal monitoring for each respiratory virus spike protein, the responses to buffer and clinical virus transport medium (CTM) were confirmed by injecting buffer without any respiratory virus spike protein, and there was no meaningful response (gray line). The neuropilin-1 receptonics, however, displayed a certain response toward the SARS-CoV-2 spike protein in the range of 1 fg μL^{-1} to 10 ng μL^{-1} (Figure 2c). The variance in current was immediately observed after SARS-CoV-2 spike protein injection, and saturated under the concentration of 1 ng μL^{-1}. Herein, the normalized sensitivity was calculated from the current variance by Equation (1) (details in Supporting Information).

The neuropilin-1 receptonics showed a detection range of 10 fg μL^{-1} to 1 ng μL^{-1} and an LOD of 10 fg μL^{-1}. Interestingly, the ACE2 receptonics were able to detect 2 types of SARS virus, responding to both SARS-CoV (blue line) and SARS-CoV-2 (red line) spike proteins. The detection performance is shown as real-time monitoring (Figure 2d). The LODs were 1 fg μL^{-1} for both species and the detection time was rapid, less than 10 sec. Although the ability of ACE2 receptonics to detect SARS-CoV-2 was 10 times higher than that of the neuropilin-1 receptonics, the sensitivity differed by ≈4 times at 10 fg μL^{-1} owing to the different binding affinity (determined based on the biosimulation). In addition, different sensitivities of the ACE2 receptonics were observed for SARS-CoV and SARS-CoV-2, indicating an interaction energy difference between ACE2 receptonics and the different SARS family spike proteins. DPP4 receptonics were introduced for the discrimination of MERS-CoV, and the performance showed a detection range from 10 fg μL^{-1} to 10 ng μL^{-1} (Figure 2e). The LOD was 10 fg μL^{-1} and the response time was

less than 10 s. Based on the results, ACE2 receptonics had a lower detection limit (1 fg μL^{-1}) than the other receptonics, and the DPP4 receptonics exhibited lower sensitivity, as indicated by the LOD.

Following the sensitivity of the device, the selectivity was also checked with real-time monitoring by injection of the spike protein of pandemic respiratory viruses, such as SARS-CoV, SARS-CoV-2, MERS-CoV, and H1N1 (influenza), into multichannel receptonics (Figure 2f). The nontarget viruses were injected at 10^3 times higher concentrations (10 pg μL^{-1}) than the target virus (10 fg μL^{-1}) to observe their influence on the detection.

Although the neuropilin-1 receptonics showed reasonable selective detection of SARS-CoV-2 (≈0.21%), it produced no response for H1N1, MERS-CoV, or SARS-CoV. In addition, H1N1 and MERS-CoV presented no interaction with the ACE2 receptonics, whereas the signal from the device gradually increased upon interaction with SARS-CoV (≈0.13%) and SARS-CoV-2 (to ≈0.53%) owing to the specific binding sites in the ACE2 receptor sequence. The increased sensitivity was, thus, correlated with the results of real-time monitoring. The specificity test toward DPP4 receptors was performed using various respiratory virus strains, and the selective interaction of DPP4 with MERS-CoV presented a sensitivity of ≈0.13%. In particular, the sensitivity of all the receptonics to the target viruses corresponded with the results of each real-time monitoring, which confirmed that there was no interference effect from the nontarget viruses.

To investigate the binding affinities, dose–concentration curves were obtained from the real-time monitoring (Figure 2g). The normalized sensitivity (N) was calculated from the interaction between virus and ND using the Langmuir isotherm equation as follows:

$$N = \frac{C}{((1/K) + C)} \tag{2}$$

where C and K indicate the concentrations of the target virus spike protein and the equilibrium constant based on the Langmuir isotherm model. The K values of each receptor were determined by curve fitting and were 0.4485 μL pg^{-1} for neuropilin-1, 4.4039 μL pg^{-1} (SARS-CoV-2) and 1.2519 μL pg^{-1} (SARS-CoV) for ACE2, and 0.2668 μL pg^{-1} for DPP4.

Figure 2h represents the real-time response of the multichannel receptonics to the various respiratory virus strains. The buffer solution (CTM) was injected into the chamber of the integrated receptonics prior to virus injection, and the current level was stably maintained for 100 s. Then, each virus was injected, resulting in current changes. Based on the results, each target virus was detected by its corresponding receptor, and a slightly decreased sensitivity to SARS-CoV-2 was observed for the Neruopilin and ACE2 receptonics due to the decrease in interaction amounts. However, the response sensitivity was similar to those exhibited in the real-time results, and the electrical signal variance corresponded to the concentration determined in real-time monitoring. Therefore, multichannel receptonics can be utilized for the simultaneous distinction detection of respiratory viruses.

For the long-term stability of each device, the time-dependent change in performance was checked in terms of the reproducibility, repeatability, and storage stability over 1 month (n = 5)

**ADVANCED
SCIENCE NEWS**

www.advancedsciencenews.com

**ADVANCED
MATERIALS**

www.advmat.de

Table 1. Amino acid mutations of receptor binding domain in SARS-CoV-2 variants of concern. (Information adapted from https://www.cdc.gov/coronavirus/2019-ncov/variants/variant-classifications.html).

Variant	Pango Lineage	Mutation
Wild type (Wuhan-Hu-1)	-	-
Alpha	B.1.1.7 and Q lineages	N501Y
Delta	B.1.617.2 and AY lineages	K417N, L452R, T478K
Omicron	B.1.1.529, BA.1, BA.1.1, BA.2, BA.3, BA.4, and BA.5 lineages	G339D, S371L, S373P, S375F, K417N, N440K, G446S, S477N, T478K, E484A, 1493R, G496S, Q498R, N501Y, Y505H

(Figure 2i). The performance of all receptonics in terms of LOD was maintained at over 99.2% until 25 days. Although the performance decreased slightly after 26 days, the sensitivity was maintained at over 98.6% for all receptonics. These results demonstrated the excellent properties of NDs owing to the structural stability of the receptor.[44]

2.3. Predicted Changes in Binding Affinity of SARS-CoV-2 Variants

We performed protein–protein interaction simulations for hACE2 or neuropilin-1 (NRP1) with the RBD (Receptor Binding Domain) of wild-type SARS-CoV-2, Alpha, Delta and Omicron variants using the AutoDock Vina. The 3D structures of the SARS-CoV-2 variant, hACE2 and neuropilin-1 were obtained from SWISS-MODEL according to PDB and NCBI. There are RBD residues of SARS-CoV-2 in direct contact with hACE2 with strong interactions at the binding interface, and the ACE2 region surrounding the ACE2 a1 helix and the C-terminus of the b3-b4 strand is less resistant to polar residues, whereas the amino acids at the N-terminus of a1 and the C-terminus of a2 are preferentially hydrophobic. It has been studied by X-ray crystallographic that the open states of the SARS-CoV-2 S1 protein domain of the spike glycoprotein involve amino acids TYR449, TYR453, ALA475, ASN487, TYR489, GLN493, GLU496, THR500, ASN501, GLU502 and TYR505, and these amino acids interacted with SER19, GLN24, LYS31, HIS34, GLU35, GLU37, ASP38, TYR41, TYR83, and LYS353 amino acids of the ACE2 surface.[45] The Alpha, Delta and Omicron variants have mutation residues in RBD which is binding with ACE2 (**Table 1**).

Furthermore, the binding site selection of SARS-CoV-2 variants for high binding signals reflects not only their affinity but also their presentation of a folded structure recognized by SARS-CoV-2. Whether these mutations in SARS-CoV-2 selectively stabilize the local structure of virus-recognized in ACE2 compared to the overall protein fold is unclear.[46] For comparison to binding affinity and residues of SARS-CoV-2 variants with ACE2(1R42) and NRP-1 (PDB ID: 1KEX), structures were predicted using Swiss Model and docked respectively. The domain's binding residue was constructed according to previous studies showing that the SARS-CoV-2 RBD is located between residues 331–526 of the S1 domain and can bind to ACE2[47,48] and residues 679 to 685 of S1 CendR peptide can bind to NRP-1.[16]

As shown in **Figure 3**, while simulations have revealed residues K417 to Y505 (-3.8 kcal mol^{-1}) and N679 to R685 (-1.4 kcal mol^{-1}) of RBD of the SARS-CoV-2 wild type contacts with human ACE2 and NRP-1, respectively. Next, we de-termined the difference in binding residues and energy using the SARS-CoV-2 Alpha, Delta and Omicron variants. RBDalpha-ACE2, RBDdelta-ACE2 and RBDomicron-ACE2 composites exhibited RMSD values ranging from 1 to 3.9 Å. The binding energies for the RBDalpha-ACE2 structure is -3.6 kcal mol^{-1}, RBDdelta-ACE2 structure is -3.7 kcal mol^{-1} and RBDomicron-ACE2 structure is -3.7 kcal mol^{-1}. For the RBD of SARS-CoV-2 with NRP-1 interaction, RBDalpha-NRP-1, RBDdelta-NRP-1, and RBDomicron-NRP-1 composites exhibited RMSD values ranging from 1 to 5.4 Å. The binding energies for the RBDalpha-NRP-1 structure is -2.2 kcal mol^{-1}, RBDdelta-NRP-1 structure is -2.4 kcal mol^{-1} and RBDomicron-NRP-1 structure is -1.3 kcal mol^{-1}. These results confirmed that the SARS-CoV-2 Alpha variant displays weaker RBD-ACE2 interaction than SARS-CoV-2, SARS-CoV-2 Delta, and SARS-CoV-2 Omicron. But all SARS-CoV-2 variants bind to ACE is still stronger than NRP-1 binding affinities.

2.4. Investigation of SARS-CoV-2 Clinical Isolates and Primate Models

To conduct the performance test, cultured variants of SARS-CoV-2 virus solution were applied to our portable device (**Figure 4**a–c). Two different SARS-CoV-2 strains (Alpha, B.1.1.7 and Delta, B.1.617.2) were isolated from standard virus solution. The prepared standard virus solution in cultured cells was diluted serially and applied to the ACE2 nanodisc immobilized graphene channel. The Alpha variant and Delta variant samples induced similar discernible current changes under 10^3 PFU mL^{-1}. The detection limit was lower than that of lateral flow assay (LFA) strips (limit of detection: 10^4 PFU mL^{-1}) (Figure S5, Supporting Information). To verify the detection performance in samples from infected primates, each cultured virus solution of 10^3 PFU mL^{-1} was mixed with macaque saliva solution. Although, the detection results presented a high-intensity noise signal generated by other biomaterials contained in the saliva solution, our newly developed receptonics device showed stable performance maintaining the current intensity compared to the reference current at values of 0.76 (Alpha) and 0.60 (Delta). The detection results showed a significant current change in the presence of saliva solution, indicating that our device can be applied to clinical samples. As of September of 2022, the only SARS-CoV-2 variant designated as a VOC is the Omicron variant (B.1.1.529). Among several SARS-CoV-2 variants, the most highly contagious strains are Omicron-based.[49,50] To verify the reactivity of our platform to Omicron, the cultured virus solution was applied and the sample was detected at a concentration of 10^1 PFU mL^{-1} (Figure 4d). The ACE2

ADVANCED
SCIENCE NEWS

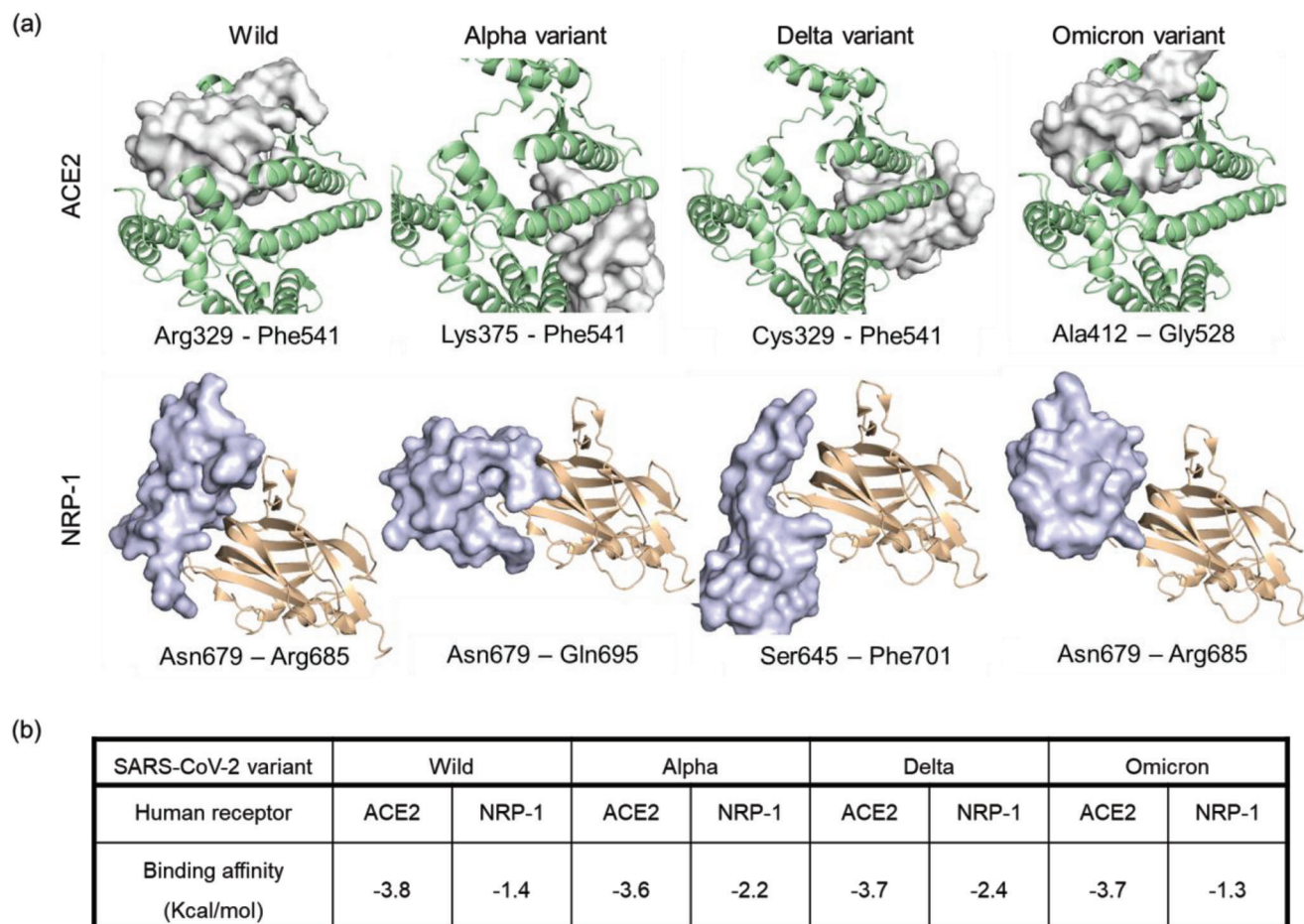www.advancedsciencenews.com

ADVANCED
MATERIALS

www.advmat.de

Figure 3. Simulated Interactions between three SARS-CoV-2 spike RBDs and the human ACE2 or human NRP1 b1 domains by Autodock. a) Docking model of the interaction RBD of SARS-CoV-2 wild-type, Alpha, Delta, and Omicron with ACE2 (top panel, ACE2: green) or NRP-1 (bottom panel NRP-1: Wheat). b) Comparison of the binding affinities of the SARS-CoV-2 variants with ACE2/NRP-1.

receptor reacted to both wild-type and variant strains and the results were consistent with those of the simulation.

Nasopharyngeal swabs collected from patients showing symptoms of COVID-19 were tested with conventional diagnostic methodologies (LFA and reverse transcription polymerase chain reaction (RT-PCR)) and the results were compared to those by our novel diagnosis platform. The clinical samples were obtained and stored in CTM. The solution was applied to our newly developed platform consisting of a receptor, graphene transistor, and printed circuit board (PCB). The technologies most commonly utilized to confirm the amount of virus in clinical sample solutions are LFA and RT-PCR. The RNA contained in CTM was extracted and purified. The prepared samples were amplified through multiple thermal cycles, and the C_T value was determined (Figure S6, Supporting Information). Although RT-PCR is highly sensitive, it has a few limitations, such as a long operation time, the need for a trained operator, and a high cost per analysis.[51] In contrast to the case for RT-PCR analysis, in LFA, the CTM itself is applied to the LFA strips to confirm the presence of the antigen (virus) through antibody–antigen recognition method. Immunoassay reaction-based methodologies provide rapid output of the diagnosis results, and the cost of di-

agnosis is relatively low.[52–53] However, its sensitivity and repeatability are insufficient for standardization. The LOD of the LFA strips was above the C_T value of 18.4 with the naked eye (Figure S7, Supporting Information). Clinical samples containing lower amounts of virus yielded false-negative signals; 37 of 61 samples from patients known to be RT-PCR positive generated false-negative results. The discernibility ratio of the test line to the control line was over 0.21 (results of clinical sample #595). Thus, a great improvement in detection performance was shown by our newly developed nanodisc-immobilized graphene transistor-based diagnosis platform.

The verified diagnosis platform was applied to 100 clinical samples suspicious for SARS-CoV-2, including multiple variants; wild type (43 samples), Omicron (12 samples), Delta (3 samples), and unknown (3 samples). The range of C_T values of those SARS-CoV-2 cohorts ranged from 9.8 to 39.2, and the median C_T value was 20.02. The samples were then classified according to C_T values. As shown in Figure 4e, the lowest C_T values were found in the Delta variants, and higher C_T values were found for the wild-type samples. The newly developed ACE2 nanodisc immobilized diagnosis platform showed significant signal changes regardless of the tested variant or the contained amount of virus
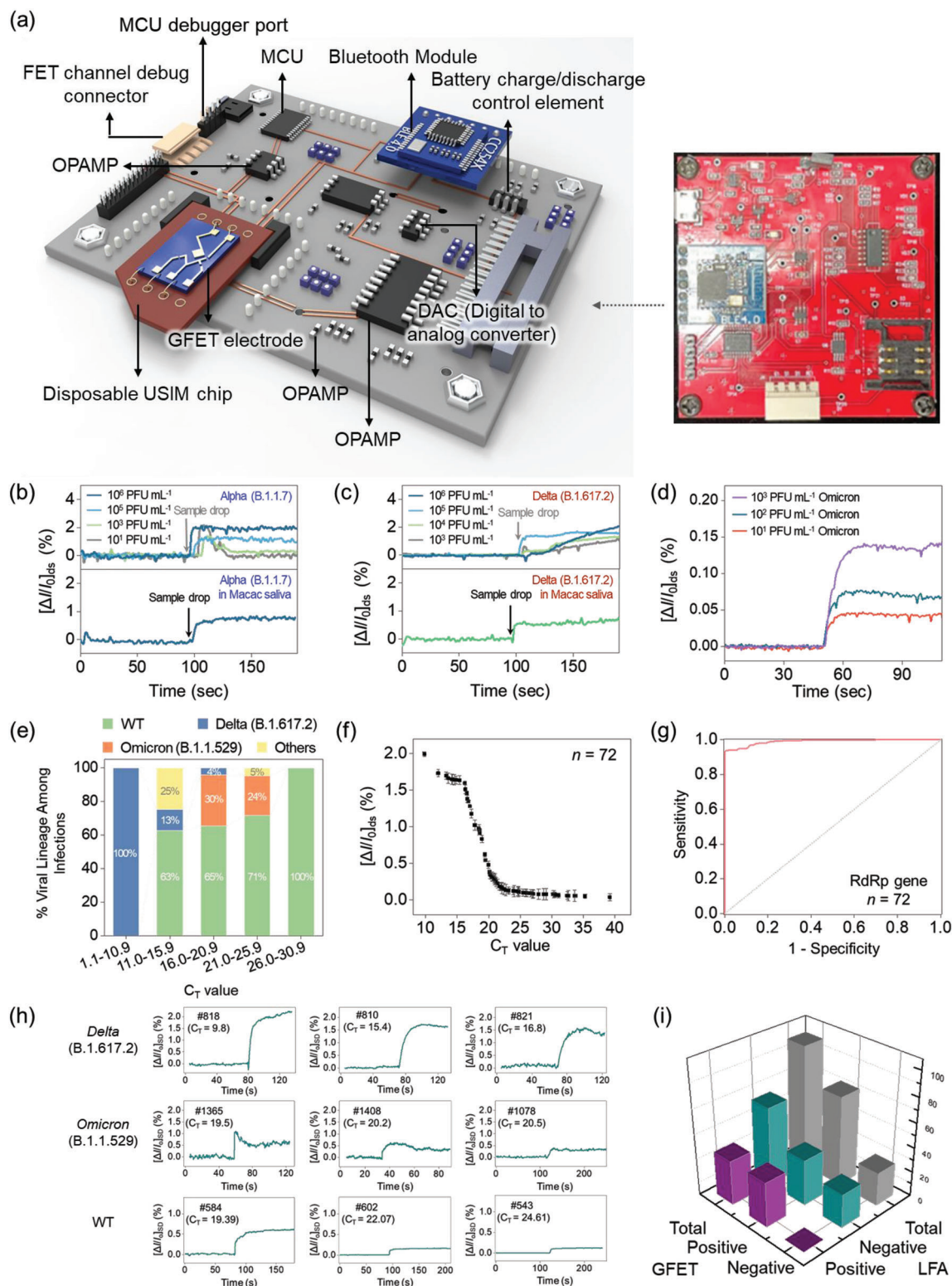
2303079 (8 of 12)

**ADVANCED
SCIENCE NEWS**

www.advancedsciencenews.com

**ADVANCED
MATERIALS**

www.advmat.de

Figure 4. Various diagnosis results of SARS-CoV-2-infected clinical samples and primate models with receptonics device. a) The portable diagnosis platform of receptonics device. b,c) Measurement of cultured SARS-CoV-2 virus solution (top: Alpha/Delta variant, bottom: Alpha/Delta variant in macaque saliva). d) Measurement of cultured Omicron variant (concentrations range from 10^1 to 10^3 PFU mL^{-1}). e) Bar graph presenting various species of SARS-CoV-2 (Delta, Omicron, WT, and others; not classified) showing the dependence of the C_T value on the variant type. f) Comparison of the detection results of 72 SARS-CoV-2-positive and SARS-CoV-2-negative clinical samples. g) ROC curve of GFET results (****$p < 0.0001$). h) Sensing results of samples from SARS-CoV-2-infected patients. i) Bar graph comparing the diagnostic results of two diagnostic formats (LFA and receptonics).

in the sample (Figure 4f,h; Figure S9, Supporting Information). Receiver operator characteristic (ROC) analysis was carried out to evaluate the performance of the receptonics-based platform as well, and the results showed a high performance of 93.85% sensitivity, 99.48% specificity, 99.2% diagnostic accuracy, and 0.52% standard error for 72 SARS-CoV-2 clinical samples (Figure 4g). The results of another on-site diagnosis platform, LFA, were compared with those from our receptonics device (Figure 4i). Among 100 SARS-CoV-2-positive clinical samples, LFA strips showed 37 false-negative results due to their low sensitivity compared to RT-PCR and receptonics. The graph demonstrates much better diagnostic capability in receptonics.

3. Conclusion

This work presented a simple and rapid diagnostic tool that uses a receptor-integrated portable device to monitor pathogens that present high potential for infection. We developed a rapid and precise on-site diagnostic platform based on receptor–ligand dynamics to discriminate among various respiratory syncytial viruses simultaneously. The docking model of the interaction between the spike protein and receptor showed that each variant binds to different binding sites of the receptor with diverse affinities. Our platform was clinically validated with various respiratory virus strains showing highly stable and specific performance, even in the presence of various interferential materials, with the passivation of interfacing compounds (N-heterocyclic carbene). Our platform provides a novel diagnostic tool that can be used to achieve early prevention of highly contagious disease. With our approach, clinical samples from patients at a very early stage of infection could potentially be screened, enabling the facile early identification of individuals who have increased amounts of virus in their bodies. Our approaches utilize the human receptor associated with the infection process in clinical samples, preventing the broad contagion of fatal disease.

4. Experimental Section

DFT Simulation: The geometry of single-layer graphene was optimized using 24 carbon atoms in the Avogadro program; the simulation was carried out via by using the 3LYP/6-31G(d) function of Gaussian 09w. Orbital gap and EDDM were performed using the molecular orbitals and surface function in Avogadro.

Nanodisc of ACE2, DPP4, and Neuropilin-1: The plasmid of ACE2, DPP4, and neuropilin-1 for cloning of recombinant protein was synthesized from BioBasic. Each sample was optimized for protein expression in *E. coli* and contained a histidine tag (HHHHHH) for purification. The protein was overexpressed in *E. coli* according to the manufacturer's protocol and then extracted using 20 mM sodium phosphate buffer pH 7.4 containing 1 mM PMSF with 1% Triton X-100. After that, the ACE2, DPP4 and neuropilin-1 were purified using the 5 mL HisTrap High-Performance His-tag protein purification column (GE Healthcare) with ÄKTA Avant 150 protein chromatography system (Gelifesciences, USA). Finally, the purified samples eluted the imidazole contained buffer (40 mM Tris/HCl, 0.3 M NaCl, 0.3 M imidazole) and then dialyzed with 10 mM Tris/HCL (pH 7.4), 0.1 M NaCl, 1 mM EDTA. The samples were filtered and concentrated using 0.22 µm syringe filter and stored at 4 °C with 0.01% NaN₃. The purified proteins were confirmed by western blotting with anti-histidine and Coomassie blue. Then, the ACE2, DPP4, and neuropilin-1 were reconstituted into nanodisc using a 1:1:100 molar ratio of purified sample:MSP (membrane scaffold protein):lipid (1:1 ratio of POPS:POPG), following an

established protocol.[54] For homogeneously sized nanodisc, separated in the size-exclusion chromatography (Superdex 200 Increase 10/300, GL, GE Healthcare). Finally, the samples were concentrated to 10–20 µM by Amicon Ultra-0.5 centrifugal filter devices (Millipore) and stored in 20 mM Tris (pH 7.4), 0.1 M NaCl, 0.5 mM EDTA, 0.01% NaN₃ and stored at 4 °C.

Cyclic Voltammetry Measurements: The CV 3-electrodes (working, counting, and reference) were fabricated by a microelectromechanical system (MEMS). The reference electrode was treated using Ag/AgCl reference ink, and the working electrode consisted of the graphene micropatterned (100 µm²). The Au line of each electrode was passivated using SiO_2 for noise prevention on Au layer, the graphene micropatterned surface was modified by NHC covalent bonding and ethynyl ferrocene. CV and EIS measurements were performed by PalmSens4 (PalmSens BV) in 0.1 mM NaClO₄ solution (scan rate: 0.1 V s⁻¹).

Fabrication of Receptonics: Chemical vapor deposition (CVD)-based large-area graphene (8 × 8 cm) was fabricated on Cu foil by protocol of the previous our studies. CVD graphene was transferred to a 4-inch SiO_2 wafer through wet-transfer process. The electrodes were fabricated by MEMS, the graphene micropatterning was performed using AZ GXR-601 photoresist coating, photolithography, and reactive-ion etching (RIE) process. The formation of gold electrodes was carried out through DNR L300-40 photoresist, photolithography, and E-beam deposition (Cr 8 nm, Au 80 nm), and the passivation layer was formed by deposition using SiO_2. The GM electrodes were dipped in NHC solution of 10 µM in vacuum for 8 h, THF, MeOH, and DW were used for surface washing of the residual NHC solution. Each ND of 4 µM was interaction on the NHC-treated GM electrodes via click reaction using 4 µM BCN-NHS click reaction agent for 4 h. The NDs immobilized GM electrodes were washed using PBS and DW for removement of non-interacted NDs.

Electrical Measurements of the Receptonics: All electrical measurements were performed using a source meter (Keithley 2612 A), the sensitivity was calculated by the normalization using the following equation

$$\left[\frac{\Delta I}{I_0}\right] = \frac{(I/I_0)}{I_0} \tag{3}$$

where I and I_0 are the measured current and the initial current value.

Simulation of Protein–Protein Interaction: The 3D homology models were constructed by the SWISS-MODEL workspace (https://swissmodel.expasy.org) using the NCBI database. The created PDB files were used to confirm protein–protein interaction (PPI) and binding affinity in ACE2 and neuropilin-1(NRP-1) with SARS-CoV-2 (Wild type, Alpha/Delta/Omicron variants). The virtual screening was carried out to confirm the various binding site and was calculated using Auto Dock Vina, version 1.1.2. and visualized using PyMOL.

Cryo-EM Imaging: For the sampling for cryo-TEM, purified SARS-CoV-2 spike and ACE2 proteins were mixed at the molar ratio of 1:1 and incubated for 2 h at 4 °C. On the surface of clean grid, 3.2 µL of protein–receptor complex was applied. Using a Vitrobot 218 Mark IV (Thermo Fisher), the sample was loaded on the Quantifoil Holey Carbon R1.2/1.3 300 mesh grids at a temperature of 25 °C and humidity level of 30% and then vitrified in liquid nigtrogen after blotting for 3.5 s with a blot force of 2 with waiting 9 s. The prepared samples were analyzed with cryo-field-emission TEM (200kV, Glacios).

Preparation of Virus Culture Solutions and SARS-CoV-2-Infected Non-Human Primate Model: The SARS-CoV-2 strains (NCCP no. 43326 for the S clade [A, 19B], NCCP no. 43345 for the GH clade [B.1, 20C] and NCCP no. 43408 for the GRA clade [Omicron, BA.1]) were obtained from the National Culture Collection for Pathogens (Cheongju, Republic of Korea). To propagate the viruses, Vero cells (CCL-81; American Type Culture Collection) were used following established protocols.[55] These cells were inoculated with SARS-CoV-2 virus for 1 h at 37 °C under 5% CO_2. Subsequently, the inoculated cells were cultured in Dulbecco's modified Eagle's medium with 2% fetal bovine serum and 1% PenStrep. Cytopathic effects were observed at day 3 post-infection, and the supernatants were harvested. Viral titers were determined using either the TCID50 (50% tissue culture infective dose) assay or plaque forming assay, as previously described.[56,57] All experiments involving the virus or infectious samples

**ADVANCED
SCIENCE NEWS**

www.advancedsciencenews.com

**ADVANCED
MATERIALS**

www.advmat.de

strictly adhered to biosafety guidelines and were conducted within a class II biosafety cabinet in the ABL-3 facility at the Korea Research Institute of Bioscience and Biotechnology (KRIBB). These experiments were authorized by permit number KRIBB-IBC-20200206.

To perform viral challenges and collect saliva samples, rhesus macaques were anesthetized using a combination of ketamine sodium (10 mg kg^{-1}) and tiletamine/zolazepam (5 mg kg^{-1}). The animals were primarily exposed to SARS-CoV-2 (S clade or GH clade) through a combination of routes, including intratracheal, oral, conjunctival, and intranasal routes, as previously detailed.[56,57] Saliva samples from infected macaques was collected at 1 day post infection (dpi) by gently aspirating them from the floor of the mouth using a syringe without a needle. All collected samples were then subjected to centrifugation and stored at −80 °C until further analysis. Ethical approval for all animal procedures was obtained from the KRIBB Institutional Animal Care and Use Committee, under permit numbers KRIBB-AEC-20226 and KRIBB-AEC-20318.

Analysis of Clinical Samples with LFA and RT-PCR: For the comparison of conventional diagnosis methodologies, nasal swabs collected from Kyungpook National University were applied to LFA and RT-PCR. The extraction of RNA was conducted with 140 μL aliquots of clinical samples using RNA extraction kit (QIAamp Viral RNA Mini Kit, QIAGEN) following the provided protocol. Each sample was analyzed with RT-PCR solution (Allplex SARS-CoV-2 Assay, Seegene) for the confirmation of C_T value. A total of 100 samples were constituted as the cohorts, including various species of SARS-CoV-2 variants. To verify the limit of detection of LFA, 100 μL aliquots of each sample was applied to the LFA strip. Within 15 min, the solution flow through the membrane and result was presented on the test line.

Diagnosis of SARS-CoV-2-Infected Macac Saliva Sample using a Portable GFET: SARS-CoV-2 virus cultured solution and clinical samples were applied to the each bioprobe-immobilized graphene FET (GFET) for the confirmation of the reaction between receptor and coronavirus spike (S) protein. The cultured virus solution such as GH clade, S clade, and Omicron was diluted with PBS and primate saliva sample. As the clinical samples injects to the graphene channel, the change of current was presented dependent on the amount of virus. The current was increased proportional to the concentration of the samples and the value was normalized with Equation (3).

Supporting Information

Supporting Information is available from the Wiley Online Library or from the author.

Acknowledgements

Conflict of Interest

The authors declare no conflict of interest.

Data Availability Statement

The data that support the findings of this study are available from the corresponding author upon reasonable request.

Keywords

[1] V. Alfano, S. Ercolano, *Appl. Health Econ. Health Policy* **2020**, *18*, 509.

[2] World Health Organization, coronavirus, https://who.int/health-topics/coronavirus, (accessed: January 2020).

[3] CDC, COVID-19, https://www.cdc.gov/coronavirus/2019-ncov (accessed: February 2021).

[4] Y. Wang, C. Liu, C. Zhang, Y. Wang, Q. Hong, S. Xu, Z. Li, Y. Yang, Z. Huang, Y. Cong, *Nat. Commun.* **2022**, *13*, 871.

[5] Yale Medicine, Omicron, Delta, Alpha, and More: What To Know About the Coronavirus Variants, https://www.yalemedicine.org/news/covid-19-variants-of-concern-omicron, (accessed: December 2021).

[6] K. A. Twohig, T. Nyberg, A. Zaidi, S. Thelwall, M. A. Sinnathamby, S. Aliabadi, S. R. Seaman, R. J. Harris, R. Hope, J. Lopez-Bernal, E. Gallagher, A. Charlett, D. De Angelis, A. M. Presanis, G. Dabrera, *Lancet Infect. Dis.* **2022**, *22*, 35.

[7] Nature, Daily Briefing: Why the Delta Variant Spreads So Fast, https://www.nature.com/articles/d41586-021-02032-5 (accessed: 22 July 2021).

[8] B. Li, A. Deng, K. Li, Y. Hu, Z. Li, Y. Shi, Q. Xiong, Z. Liu, Q. Guo, L. Zou, H. Zhang, M. Zhang, F. Ouyang, J. Su, W. Su, J. Xu, H. Lin, J. Sun, J. Peng, H. Jiang, P. Zhou, T. Hu, M. Luo, Y. Zhang, H. Zheng, J. Xiao, T. Liu, M. Tan, R. Che, H. Zeng, *Nat. Commun.* **2022**, *13*, 460.

[9] S. S. A. Karim, Q. A. Karim, *Lancet* **2021**, *398*, 2126.

[10] Y. Tang, J. E. Schmitz, D. H. Persing, C. W. Stratton, *J. Clin. Microbiol.* **2020**, *58*, https://doi.org/10.1128/jcm.00512-20.

[11] J. Shang, G. Ye, K. Shi, Y. Wan, C. Luo, H. Aihara, Q. Geng, A. Auerbach, F. Li, *Nature* **2020**, *581*, 221.

[12] M. Cevik, K. Kuppalli, J. Kindrachuk, M. Peiris, *BMJ [Br. Med. J.]* **2020**, *371*, m3862.

[13] G. Iacobellis, *Diabetes Res. Clin. Pract.* **2020**, *162*, 108125.

[14] N. Wang, X. Shi, L. Jiang, S. Zhang, D. Wang, P. Tong, D. Guo, L. Fu, Y. Cui, X. Liu, K. C. Arledge, Y. H. Chen, L. Zhang, X. Wang, *Cell Res.* **2013**, *23*, 986.

[15] Q. Zhang, R. Xiang, S. Huo, Y. Zhou, S. Jiang, Q. Wang, F. Yu, *Signal Transduction Targeted Ther.* **2021**, *6*, 233.

**ADVANCED
SCIENCE NEWS**

www.advancedsciencenews.com

**ADVANCED
MATERIALS**

www.advmat.de

[16] J. L. Daly, B. Simonetti, K. Klein, K. E. Chen, M. K. Williamson, C. Antón-Plágaro, D. K. Shoemark, L. Simón-Gracia, M. Bauer, R. Hollandi, U. F. Greber, P. Horvath, R. B. Sessions, A. Helenius, J. A. Hiscox, T. Teesalu, D. A. Matthews, A. D. Davidson, B. M. Collins, P. J. Cullen, Y. Yamauchi, *Science* **2020**, *370*, 861.

[17] L. Cantuti-Castelvetri, R. Ojha, L. D. Pedro, M. Djannatian, J. Franz, S. Kuivanen, F. van der Meer, K. Kallio, T. Kaya, M. Anastasina, T. Smura, L. Levanov, L. Szirovicza, A. Tobi, H. Kallio-Kokko, P. Österlund, M. Joensuu, F. A. Meunier, S. J. Butcher, M. S. Winkler, B. Mollenhauer, A. Helenius, O. Gokce, T. Teesalu, J. Hepojoki, O. Vapalahti, C. Stadelmann, G. Balistreri, M. Simons, *Science* **2020**, *370*, 856.

[18] F. Ali, A. Kasry, M. Amin, *Med. Drug Discovery* **2021**, *10*, 100086.

[19] B. Cosar, Z. Y. Karagulleoglu, S. Unal, A. T. Ince, D. B. Uncuoglu, G. Tuncer, B. R. Kilinc, Y. E. Ozkan, H. C. Ozkoc, I. N. Demir, A. Eker, F. Karagoz, S. Y. Simsek, B. Yasar, M. Pala, A. Demir, I. N. Atak, A. H. Mendi, V. U. Bengi, G. Cengiz Seval, E. Gunes Altuntas, P. Kilic, D. Demir-Dora, *Cytokine Growth Factor Rev.* **2022**, *63*, 10.

[20] M. K. Annavajhala, H. Mohri, P. Wang, M. Nair, J. E. Zucker, Z. Sheng, A. Gomez-Simmonds, A. L. Kelley, M. Tagliavia, Y. Huang, T. Bedford, D. D. Ho, A.-C. Uhlemann, *medRxiv* **2021**, 21252259.

[21] N. Shahhosseini, G. Babuadze, G. Wong, G. P. Kobinger, *Microorganisms* **2021**, *9*, 926.

[22] K. H. Kim, S. J. Park, C. S. Park, S. E. Seo, J. Lee, J. Kim, S. H. Lee, S. Lee, J. S. Kim, C. M. Ryu, D. Yong, H. Yoon, H. S. Song, S. H. Lee, O. S. Kwon, *Biosens. Bioelectron.* **2020**, *167*, 112514.

[23] K. H. Kim, C. S. Park, S. J. Park, J. Kim, S. E. Seo, J. E. An, S. Ha, J. Bae, S. Phyo, J. Lee, K. Kim, D. Moon, T. H. Park, H. S. Song, O. S. Kwon, *Biosens. Bioelectron.* **2022**, *200*, 113908.

[24] O. S. Kwon, K. H. Kim, S. E. Seo, C. S. Park, S. Kim, S. Lee, C.-M. Ryu, D. Yong, Y. M. Park, *Angew. Chem., Int. Ed.* **2022**, *61*, 202209726.

[25] W. Zhao, B. Xia, L. Lin, X. Xiao, P. Liu, X. Lin, H. Peng, Y. Zhu, R. Yu, P. Lei, J. Wang, L. Zhang, Y. Xu, M. Zhao, L. Peng, Q. Li, W. Duan, Z. Liu, S. Fan, K. Jiang, *Sci. Adv.* **2017**, *3*, 1603231.

[26] A. Inayeh, R. R. K. Groome, I. Singh, A. J. Veinot, F. C. de Lima, R. H. Miwa, C. M. Crudden, A. B. McLean, *Nat. Commun.* **2021**, *12*, 4034.

[27] Y. Zeng, T. Zhang, M. R. Narouz, C. M. Crudden, P. H. McBreen, *Chem. Commun.* **2018**, *54*, 12527.

[28] C. K. Wolfgang, A. Herrmann, *Angew. Chem., Int. Ed.* **1997**, *36*, 2162.

[29] O. S. Kwon, S. H. Lee, S. J. Park, J. H. An, H. S. Song, T. Kim, J. H. Oh, J. Bae, H. Yoon, T. H. Park, J. Jang, *Adv. Mater.* **2013**, *25*, 4177.

[30] O. S. Kwon, H. S. Song, S. J. Park, S. H. Lee, J. H. An, J. W. Park, H. Yang, H. Yoon, J. Bae, T. H. Park, J. Jang, *Nano Lett.* **2015**, *15*, 6559.

[31] A. C. Ferrari, J. C. Meyer, V. Scardaci, C. Casiraghi, M. Lazzeri, F. Mauri, S. Piscanec, D. Jiang, K. S. Novoselov, S. Roth, A. K. Geim, *Phys. Rev. Lett.* **2006**, *97*, 187401.

[32] P. May, M. Lazzeri, P. Venezuela, F. Herziger, G. Callsen, J. S. Reparaz, A. Hoffmann, F. Mauri, J. Maultzsch, *Phys. Rev. B: Condens. Matter Mater. Phys.* **2013**, *87*, 75402.

[33] J.-B. Wu, X. Zhang, M. Ijäs, W. P. Han, X. F. Qiao, X. L. Li, D. S. Jiang, A. C. Ferrari, P. H. Tan, *Nat. Commun.* **2014**, *5*, 5309.

[34] A. C. Ferrari, D. M. Basko, *Nat. Nanotechnol.* **2013**, *8*, 235.

[35] D. B. Vidano, R. P. Fishbach, T. M. Willis, L. J. Loehr, *Solid State Commun.* **1981**, *39*, 341.

[36] R. Poręba, A. de los Santos Pereira, R. Pola, S. Jiang, O. Pop-Georgievski, Z. Sedláková, H. Schönherr, *Macromol. Biosci.* **2020**, *20*, 1900354.

[37] F. Li, X. H. Yu, F. Y. Kong, Z. X. Wang, W. Wang, *RSC Adv.* **2017**, *7*, 31281.

[38] K. Cameron, L. Rozano, M. Falasca, R. L. Mancera, *Int. J. Mol. Sci.* **2021**, *22*, 7001.

[39] P. Zhou, X. Lou Yang, X. G. Wang, B. Hu, L. Zhang, W. Zhang, H. R. Si, Y. Zhu, B. Li, C. L. Huang, H. D. Chen, J. Chen, Y. Luo, H. Guo, R. Di Jiang, M. Q. Liu, Y. Chen, X. R. Shen, X. Wang, X. S. Zheng, K. Zhao, Q. J. Chen, F. Deng, L. L. Liu, B. Yan, F. X. Zhan, Y. Y. Wang, G. F. Xiao, Z. L. Shi, *Nature* **2020**, *579*, 270.

[40] Q. Wang, Y. Zhang, L. Wu, S. Niu, C. Song, Z. Zhang, G. Lu, C. Qiao, Y. Hu, K. Y. Yuen, Q. Wang, H. Zhou, J. Yan, J. Qi, *Cell* **2020**, *181*, 894.

[41] M. Klaewkla, T. Charoenwongpaiboon, P. Mahalapbutr, *J. Mol. Liq.* **2021**, *335*, 116537.

[42] H. Yang, D. Kim, J. Kim, D. Moon, H. S. Song, M. Lee, S. Hong, T. H. Park, *ACS Nano* **2017**, *11*, 11847.

[43] J. Oh, H. Yang, G. E. Jeong, D. Moon, O. S. Kwon, S. Phyo, J. Lee, H. S. Song, T. H. Park, J. Jang, *Anal. Chem.* **2019**, *91*, 12181.

[44] K. H. Kim, D. Moon, J. E. An, S. J. Park, S. E. Seo, S. Ha, J. Kim, K. Kim, S. Phyo, J. Lee, H.-Y. Kim, M. Kim, T. H. Park, H. S. Song, O. S. Kwon, *Biosens. Bioelectron.* **2022**, *215*, 114551.

[45] A. Banerjee, M. Kanwar, D. Santra, S. Maiti, *Transl. Med. Commun.* **2022**, *7*, 2.

[46] K. K. Chan, D. Dorosky, P. Sharma, S. A. Abbasi, J. M. Dye, D. M. Kranz, A. S. Herbert, E. Procko, *Science* **2020**, *369*, 1261.

[47] W. Tai, L. He, X. Zhang, J. Pu, D. Voronin, S. Jiang, Y. Zhou, L. Du, *Cell. Mol. Immunol.* **2020**, *17*, 613.

[48] J. Lan, J. Ge, J. Yu, S. Shan, H. Zhou, S. Fan, Q. Zhang, X. Shi, Q. Wang, L. Zhang, X. Wang, *Nature* **2020**, *581*, 215.

[49] M. Rathinasamy, S. Kandhasamy, *J. Med. Virol.* **2022**, *94*, 2414.

[50] A. Li, A. Maier, M. Carter, T. H. Guan, *J. Med. Virol.* **2022**, *94*, 1784.

[51] K. Guo, S. Wustoni, A. Koklu, E. Díaz-Galicia, M. Moser, A. Hama, A. A. Alqahtani, A. N. Ahmad, F. S. Alhamlan, M. Shuaib, A. Pain, I. McCulloch, S. T. Arold, R. Grünberg, S. Inal, *Nat. Biomed. Eng.* **2021**, *5*, 666.

[52] S. A. Taya, D. N. Alhamss, I. Colak, S. K. Patel, *Opt. Quant. Electron.* **2022**, *54*, 127.

[53] S. A. Taya, N. Doghmosh, A. Sharma, I. Colak, A. H. M. Almawgani, *Pramana – J. Phys.* **2022**, *96*, 215.

[54] S. E. Seo, S. G. Lim, K. H. Kim, J. Kim, C. J. Shin, S. Kim, L. Kim, S. H. Lee, S. Y. Jang, H. W. Oh, H. Lee, W. Kim, Y. M. Park, K. G. Lee, S. H. Lee, S. Ha, O. S. Kwon, *Adv. Mater.* **2023**, *35*, 2206198.

[55] P. S. Kwon, S. Xu, H. Oh, S. J. Kwon, A. L. Rodrigues, M. Feroz, K. Fraser, F. He, F. Zhang, J. J. Hong, R. J. Linhardt, J. S. Dordick, *Commun. Biol.* **2023**, *6*, 387.

[56] G. Kim, D. H. Kim, H. Oh, S. Bae, J. Kwon, M. J. Kim, E. Lee, E. H. Hwang, H. Jung, B. S. Koo, S. H. Baek, P. Kang, Y. J. An, J. H. Park, J. H. Park, K. S. Lyoo, C. M. Ryu, S. H. Kim, J. J. Hong, *J. Infect. Dis.* **2021**, *224*, 1861.

[57] B. S. Koo, H. Oh, G. Kim, E. H. Hwang, H. Jung, Y. Lee, P. Kang, J. H. Park, C. M. Ryu, J. J. Hong, *J. Infect. Dis.* **2020**, *222*, 1596.